Title: Temporally resolved laser induced plasma diagnostics of single crystal silicon - effects of ambient pressure.

Author names and affiliations: J.S. Cowpe*, J.S. Astin, R.D. Pilkington, A.E. Hill,

Institute for Materials Research, University of Salford, Salford, M5 4WT, UK.

j.s.cowpe@pgr.salford.ac.uk

r.d.pilkington@salford.ac.uk

j.s.astin@salford.ac.uk

a.e.hill@salford.ac.uk

***Corresponding author:** J. S. Cowpe. j.s.cowpe@pgr.salford.ac.uk

Institute for Materials Research, Room 104 Maxwell Building, University of Salford, Salford, M5 4WT, UK. Telephone: +44-161-295-5268

Abstract: Laser-Induced Breakdown Spectroscopy of silicon was performed using a nanosecond pulsed frequency doubled Nd:YAG (532 nm) laser. The temporal evolution of the laser ablation plumes in air at atmospheric pressure and at an ambient pressure of ~ 10^{-5} mbar is presented. Electron densities were determined from the Stark broadening of the Si (I) 288.16 nm emission line. Electron densities in the range of 6.91×10^{17} to 1.29×10^{19} cm^{-3} at atmospheric pressure and 1.68×10^{17} to 3.02×10^{19} cm^{-3} under

vacuum were observed. Electron excitation temperatures were obtained from the line to continuum ratios and yielded temperatures in the range 7600 – 18200 K at atmospheric pressure, and 8020 – 18200 K under vacuum. The plasma morphology is also characterized with respect to time in both pressure regimes.

Keywords: LIBS, laser ablation, plasma diagnostics, vacuum, silicon.

1. Introduction

Laser-Induced Breakdown Spectroscopy (LIBS) is a powerful optical emission spectroscopy analytical tool capable of sampling solids, liquids and gases for research and industrial applications. A pulsed laser source is employed to vaporize and excite the analyte forming a plasma. The optical emission from the relaxation of excited species within the plasma yields information regarding the composition of the material under test. Several very good review articles regarding LIBS fundamentals, applications and experimental approaches have been published [1-7]. The versatility of LIBS has seen it employed in numerous industrial [8-11], environmental [12-14] and archaeological [15-17] applications.

Spectroscopic analysis of laser-induced plasmas can lead to the determination of electron number densities from the Stark broadening of emission line profiles [18, 19]; plasma temperatures may be determined from the 2 line ratio method [18], Boltzmann plot method [20, 21] and line-to-continuum ratio method [22, 23]. Milàn and Laserna [24] performed diagnostics of silicon plasmas produced by 532 nm Nd:YAG nanosecond

pulses, in air at atmospheric pressure. Plasma temperatures determined using the Boltzmann plot method tended to remain constant with increasing delay, in the range of 6000 - 9000 K. This behaviour, contrary to their expectations, was ascribed to difficulties in finding silicon lines fulfilling the requirements of the Boltzmann plot method. Electron densities of the order 10^{18} cm^{-3} were determined from the Stark broadening of the Si (I) 250.65 nm line. Liu et al. [22] performed spectroscopic analyses of silicon plasmas induced by nanosecond Nd:YAG 266 nm pulses, in air at atmospheric pressure. Plasma temperatures were determined from the line-to-continuum ratio method in the range 20000 – 70000 K during the early phase (<300 ns) of plasma expansion. Electron densities in the range of 10^{18} -10^{19} cm^{-3} were determined from the Stark broadening of the Si (I) 288.16 nm line.

The electron densities and temperatures reported by Milàn and Laserna [24] and Liu et al. [22] for silicon plasmas are comparable to those calculated for other solid analytes in air at atmospheric pressure. Shaikh et al. report electron temperatures in Nd:YAG (532 nm) ns pulse induced zinc plasmas of approximately 9000 K determined by the 2-line method, and electron densities of the order 10^{16} cm^{-3} [18]. Drogoff et al. report electron densities of the order 10^{16} – 10^{18} cm^{-3}, and electron temperatures in the range 5500 -11000 K in Nd:YAG (1064 nm) nanosecond pulse laser induced aluminium plasmas [20]. Harilal et al. performed electron density and temperature measurements in Nd:YAG (1064 nm) laser induced plasmas at an ambient pressure of ~ 10^{-4} mbar; electron densities of the order 10^{17} cm^{-3} and temperatures in the range 17000 – 40000 K were determined [25]. Radziemski et al. conducted LIBS of geological samples in a simulated Martian

atmosphere, and reported that the appearance and characteristics of the induced plasma plumes were strongly pressure dependent [26]. Harilal et al. applied 2 ns gated ICCD photography to characterize the morphology of laser-induced aluminium plumes through a range of ambient pressures from ~ 10^{-6} to 100 mbar, confirming the general agreement of plume front expansion with various models [27].

In this paper we report the analysis of frequency doubled Nd:YAG (532 nm) nanosecond laser ablation plumes of silicon in terms of electron density and temperature profiles with respect to time using a swept gate delay for temporal resolution of the plume. Electron temperatures were calculated from the line-to-continuum ratio method using the Si (I) 288.16 nm line. Electron densities were determined from the Stark broadening of the Si (I) 288.16 nm line. Investigations were conducted in air at atmospheric pressure and at an ambient pressure p_a ~ 10^{-5} mbar, and the effect of pressure variation on the analyses is reported. Non-dispersed gated images reveal information regarding the morphology of the laser-induced plasmas with respect to time.

2. Experimental set-up

The apparatus shown in Fig. 1 is designed for LIBS material analysis and plasma plume characterisation through a range of pressure regimes, from atmosphere down to an ambient pressure , p_a < 10^{-6} mbar, and is described in more detail elsewhere [28]. The set-up includes an Nd:YAG laser (Continuum, Surelite), frequency doubled to produce an output at 532 nm, with 4-6 ns pulse length and a peak power of 200 mJ. For this investigation the laser was operated at a repetition rate of 10 Hz unless otherwise

specified. Laser radiation was focussed onto the sample surface using a 150 mm plano-convex quartz lens, with a spot size at the sample estimated as ~ 400 μm using full laser power. Samples were placed perpendicular to the laser beam.

The material under test was mounted in the vacuum chamber on a rotating stage such that each LIBS analysis may be performed on a fresh piece of the sample. A turbomolecular and rotary pump set is used to evacuate the chamber to $p_a < 10^{-6}$ mbar. A molecular sieve foreline trap was employed to reduce pump oil contamination.

Fig. 1

Optical emission from the plasma plume was collected, at 90° to the direction of laser beam propagation, through a quartz window in the vacuum chamber wall. Plasma plumes were imaged using a plano-convex quartz lens (focal length 100 mm) onto the entrance slit of an Acton Research Spectra Pro 500i 0.5 m imaging triple grating (150, 600, 2400 grooves mm^{-1}) spectrometer. Dispersed images of the plasma were captured with the spectrometer input slit width set to 10 μm, non-dispersed images were captured with a slit width of 3 mm. The spectrometer input slit was orientated to capture images along the entire plume in the direction of plume propagation; all measurements taken were thus spatially integrated along the length of the plume. The output of the spectrometer was coupled to a Princeton Instruments PI-MAX ICCD camera that utilized a proximity focussed MCP intensifier connected via a fibre-optic coupling to the CCD array. The 1024 × 256 pixel CCD array is thermoelectrically cooled to -20°C. The laser power supply, camera and PC are connected to a Princeton Instruments ST-133A

programmable timing generator, enabling temporal resolution of the plasma plume.

Standard semiconductor grade polished silicon [111] wafers were used in this study. Electron temperature and density measurements were performed with the 2400 grooves mm^{-1} grating, using the neutral Silicon (I) 288.16 nm emission line. Non-dispersed images of the plasma were collected with the 2400 grooves mm^{-1} grating positioned to allow the zero order to propagate to the ICCD. Spectral resolution when using the 2400 grooves mm^{-1} grating was 0.02 nm $pixel^{-1}$.

3. Results and discussion

Figs. 2a and 2b show the temporal evolution of the Si (I) 288.16 nm emission line intensity at atmospheric pressure and at an ambient pressure of ~ 10^{-5} mbar, respectively. The gate delay was swept from 10 to 4010 ns after laser firing, in 200 ns increments, with the gate width fixed at 200 ns to avoid overlapping information. Intensifier gain was set to 200 and each data set was the accumulation of ten spectra. When comparing Figs. 2a and 2b it is evident that the FWHM of the emission line is considerably narrower at p_a ~ 10^{-5} mbar due to free plasma expansion and a subsequent lack of pressure broadening effects. The maximum line intensity recorded under vacuum is approximately 3 times greater than at atmospheric pressure; but decays more rapidly. The continuum radiation decays more rapidly under vacuum.

Fig. 2a

Fig. 2b

3.1 Measurement of Electron Temperature, T_e.

Use of the Boltzmann plot for accurate temperature determination proved difficult; very few suitable Si (I) emission lines exist in such a narrow wavelength range that our system may capture them simultaneously. This problem has been noted previously for silicon by Milàn and Laserna [24]. The electron temperature was instead determined using the line-to-continuum ratio method [22,23], which relies on the accurate measurement of the continuum level. At delay times greater than ~ 2 μs at atmospheric pressure, and greater than ~ 1.4 μs at $p_a \sim 10^{-5}$ mbar, the continuum may no longer be resolved above the dark charge level of the ICCD. As such, this study focussed on temporal evolution of plasma plumes up to a maximum delay of 1410 ns. To employ the line-to-continuum ratio method a Lorentzian curve was fitted to each data set, as shown in Fig. 3.

Fig. 3

The Lorentz fit is expressed by Equation 1,

$$y = y_0 + \frac{2A}{\pi}.\frac{w}{4(x - x_c)^2 + w^2} \quad (1)$$

where: y_0 is the baseline offset, A represents integrated peak emission, x_c is the centre wavelength of the peak, and w the peak full width at half maximum height (FWHM). The Lorentz fit best describes the spectra, indicating negligible self absorption of the 288.16 nm Silicon (I) line under the conditions of this study; the R^2 coefficient of determination is greater than 0.9 in each case. All spectra were corrected for the spectral

response of the instrument, and the ICCD dark charge subtracted. Using the parameters resulting from the Lorentz fit to the 288.16 nm Si (I) emission line, and the assumption of Local Thermal Equilibrium (LTE) in the plasma, the electron temperature T_e may be calculated from Equation 2 [22].

$$\frac{\varepsilon_l}{\varepsilon_c}(\lambda) = C_r \frac{A_{21} g_2}{U_i} \frac{\lambda_c^2}{\lambda_l T_e} \frac{\exp\left(\frac{E_i - E_2 - \Delta E_i}{kT_e}\right)}{\left[\xi\left(1 - \exp\frac{-hc}{\lambda k T_e}\right) + G\left(\exp\frac{-hc}{\lambda k T_e}\right)\right]} \qquad (2)$$

where C_r = 2.005 x 10^{-5} (s K), A_{21} is the transition probability, E_i is the ionisation potential, E_2 is the upper state energy level, and g_2 the upper state statistical weight. ΔE_i is the lowering of the ionisation potential of atoms in the presence of a field of ions and is small enough to be deemed insignificant [22]. U_i is the partition function for a silicon ion, and G is the free-free Gaunt factor, which is assumed to be unity [22]. ξ is the free-bound continuum correction factor, and was calculated for Si vapour by Liu et al. as 1.4 [22]. The parameters used for plasma temperature determinations are summarized in Table 1.

Table 1: Parameters used for plasma temperature determination [22,30].

Transition (nm)	A_{2l} (10^8 s^{-1})	g_2	E_2 (eV)	E_i (eV)	U_i	ξ	G	C_r (sK)
Si (I) 288.16	1.9	3	5.028	8.151	6.159	1.4	1	2.005 x 10^{-5}

ε_c is the continuum emission coefficient and is equal to y_0 obtained from the Lorentz fit. ε_l is the integrated emission coefficient over the line spectral profile, and is given by the

integrated area of the fitted Lorentz curve, A. λ_c and λ_l are the continuum wavelength and line wavelength (nm) respectively; from the Lorentz curve fit: $\lambda_c = \lambda_l = x_c$.

Fig. 4

Table 2: Fit parameters and coefficients of determination, R^2, for lines of best fit from Fig. 4.

Pressure	Parameter	Value	R^2
Atmosphere	a	54611.077	0.988
	b	-0.275	
Vacuum	y_0	7496.077	0.999
	x_0	-0.560	
	A_1	12090.525	
	t_1	32.933	
	A_2	2011.645	
	t_2	490.484	

The temporal evolution of T_e calculated from spectra obtained at atmospheric pressure and at $p_a \sim 10^{-5}$ mbar is shown in Fig. 4. The dominance of the continuum radiation over line emission in the earliest stages of plasma formation and expansion leads to difficulties in accurate determination of T_e at delay times < 60 ns at atmosphere, and < 10 ns at $p_a \sim 10^{-5}$ mbar. Once the Si (I) 288.16 nm emission line becomes resolvable above the continuum radiation, the earliest measurable T_e is approximately 18200 K for both ambient pressure regimes, decreasing more rapidly under vacuum. T_e was only determined up to a delay time of 710 ns for $p_a \sim 10^{-5}$ mbar, due to the reduction in resolution of the continuum radiation above the dark charge of the ICCD. Electron excitation temperatures obtained from the line to continuum ratios were yielded in the range 7600 – 18200 K at atmospheric pressure, and 8020 – 18200 K under vacuum. The

values determined at atmospheric pressure are similar to those found by Milàn and Laserna [24] and Liu et al. [22]. At atmospheric pressure the temporal evolution of T_e best fits a power curve of the type $y = ax^b$, with values as summarized in Table 2. Under vacuum T_e is shown to best fit a second order exponential decay of the form: $y = y_0 + A_1 \times \exp(-(x-x_0)/t_1) + A_2 \times \exp(-(x-x_0)/t_2)$ with parameters as summarized in Table 2. The double phase decay of T_e hints at an initial rapid plasma temperature drop, followed by a period of slower plasma cooling under vacuum conditions [25, 27].

3.2 Determination of Electron Density, N_e.

The electron density of the laser ablation plasma was determined from the Stark broadening of the 288.16 nm Si (I) emission line. The contributions of resonance and Doppler line broadening were deemed insignificant under the conditions of this study. Resonance broadening is negligible as the 288.16 nm Si (I) line is not associated with a ground state [22, 31]. The Doppler effect will cause a broadening in line width for Si (I) 288.16 nm of less than 0.0055 nm, assuming that the plasma temperature is the maximum determined in this study. This value is estimated from Equation 3 [22].

$$w_{1/2} = 7.19 \times 10^{-10} \lambda \, (T/M)^{1/2} \qquad (3)$$

where $w_{1/2}$ is the Doppler broadening contribution in nm, λ is the line wavelength in nm, T is the plasma temperature in Kelvin, and M is the atomic mass in amu. The electron density of the plasma is related to the Stark pressure broadening of the emission lines by Equation 4 [24].

$$\Delta\lambda_{1/2} = 2w\left(\frac{N_e}{10^{16}}\right) + 3.5A\left(\frac{N_e}{10^{16}}\right)^{1/4}\left[1 - 1.2N_D^{-1/3}\right]w\left(\frac{N_e}{10^{16}}\right) \quad (4)$$

where $\Delta\lambda_{1/2}$ is the FWHM broadening of the line, N_e is the plasma electron number density, w and A are the electron impact width parameter and the ion broadening parameter respectively, and N_D the number of particles in the Debye sphere, given by Equation 5 [24],

$$N_D = 1.72 \times 10^9 \frac{T^{3/2}}{N_e^{1/2}} \quad (5)$$

where T is the plasma temperature. Due to the small ionic contribution to Stark broadening, Equation 4 may be simplified to Equation 6 [18, 24].

$$\Delta\lambda_{1/2} = 2w\left(\frac{N_e}{10^{16}}\right) \quad (6)$$

The electron impact width parameter w is temperature dependent, and was interpolated for each appropriate temperature from the values given by Griem [29]. The observed line shape must be corrected by subtracting the broadening contribution from the instrument, as shown in Equation 7 [18].

$$\Delta\lambda_{\text{true}} = \Delta\lambda_{\text{observed}} - \Delta\lambda_{\text{instrument}} \quad (7)$$

The instrumental broadening profile was found to be 0.04 nm, measured using several narrow emission lines from a cadmium hollow cathode lamp.

Fig. 5

Table 3: Fit parameters and coefficients of determination, R^2, for lines of best fit from Fig. 5.

Pressure	Parameter	Value	R^2
Atmosphere	a	3.681	0.991
	b	-0.8220	
Vacuum	y_0	1.687×10^{17}	1.000
	x_0	4.662	
	A_1	4.30×10^{19}	
	t_1	13.963	
	A_2	7.890×10^{17}	
	t_2	89.346	

Fig. 5 shows the electron densities observed at atmospheric pressure and at $p_a \sim 10^{-5}$ mbar. Calculation of N_e proved difficult for times up to 60 ns (at atmospheric pressure) as the Si (I) 288.16 nm emission line was not resolvable above the continuum. Electron densities were determined to be in the range 6.91×10^{17} to 1.29×10^{19} cm^{-3} at atmospheric pressure and $1.68 \times 10^{17} - 3.02 \times 10^{19}$ cm^{-3} under vacuum. The electron density is seen to diminish more rapidly at lower ambient pressures due to the free expansion of the plasma. As T_e is required to calculate w, N_e may not be determined at delays greater than 710 ns under vacuum. At atmospheric pressure the temporal evolution of N_e best fits a power curve with values as summarized in Table 3. Under vacuum N_e is shown to best fit a second order exponential decay with parameters as summarized in Table 3. The double phase decay of N_e hints at an initial rapid plasma

expansion, followed by a period of slower expansion under vacuum conditions [25, 27].

3.2.1 LTE requirements

In order for any given plasma to be considered to be in LTE, the lower limit for the electron number density N_e must satisfy Equation 8 [24, 31]:

$$N_e \ (\text{cm}^{-3}) \geq 1.6 \times 10^{12} \ T^{1/2} \ \Delta E^3 \qquad (8)$$

where ΔE (eV) is the energy difference between the upper and lower states and T (K) is the plasma temperature. For the Si (I) 288.16 nm line transition, ΔE = 4.3 eV. Using the highest temperature measured, T_e = 18200 K, from Equation 8 we yield a minimum electron density of $N_e \geq 1.072 \times 10^{17}$ cm^{-3} for LTE to hold. For the range of N_e determined at atmospheric pressure, 1.29×10^{19} cm^{-3} (60 ns delay) to 6.91×10^{17} cm^{-3} (1410 ns delay), N_e is greater than this lower limit and LTE may be assumed to be valid. At $p_a \sim 10^{-5}$ mbar, the range of N_e measured is 1.02×10^{19} cm^{-3} (10 ns delay) to 1.68×10^{17} cm^{-3} (710 ns delay). Here N_e is greater than the lower limit determined for valid assumption of LTE; however at delay times > 300 ns the electron density is only just greater than the lower limit and the assumption that LTE exists must be treated with caution. It should also be noted that the criterion outlined in Equation 8 is a necessary, but not entirely sufficient, condition for LTE.

3.3 Plasma morphology

Fig. 6 shows time resolved non-dispersed images of the laser–induced silicon plasmas at atmospheric pressure and at $p_a \sim 10^{-5}$ mbar. The laser was operated in single shot mode

with each shot on a clean piece of the sample; each image is normalized to its maximum intensity. To prevent ICCD spot damage from intense plasma light emission, a ND 2.0 neutral density filter was placed in front of the spectrometer input slit. The integration time was 50 ns and the intensifier gain set to 200 as in the spectroscopic measurements detailed in previous sections. The plumes are asymmetrical about the axis of laser beam propagation due to irregularities in the beam profile. It can be seen that in the early stages of plasma formation, ~ 10 ns, the plasmas generated at atmospheric pressure and at $p_a \sim 10^{-5}$ mbar are comparable in terms of size luminosity. This similarity is backed up by the spectroscopic measurements of N_e and T_e. At the earliest delay times investigated, N_e and T_e are comparable at atmospheric pressure and at $p_a \sim 10^{-5}$ mbar. However, as is evident from Fig. 6, the plasma disperses much more rapidly under lower ambient pressure due to free plasma expansion on account of an increased mean free path of the confining ambient gas; this is again supported by the spectroscopic measurements of N_e and T_e.

Fig. 6

4. Conclusion

Diagnostics of Nd:YAG (532 nm) laser-induced silicon plumes have been performed. The temporal evolution of the plumes at atmospheric pressure and at an ambient pressure of $\sim 10^{-5}$ mbar was characterized in terms of electron temperature and density. Electron temperatures were measured in the range 7600 – 18200 K at atmospheric pressure, and 8020 – 18200 K under vacuum. Electron densities in the range of 6.91×10^{17} to $1.29 \times$

10^{19} cm^{-3} at atmospheric pressure and 1.68×10^{17} to 3.02×10^{19} cm^{-3} under vacuum were observed. Spectroscopic analysis (Figs. 4 and 5) suggests that in the initial stages of plasma evolution (< 75 ns) the ambient pressure regime has little effect on the plasma characteristics; this is confirmed by the non-dispersed images of the plasma, as shown in Fig. 6. Our analysis is in line with other published data, but the authors are aware of the limitations of the LTE based approach taken.

Acknowledgements

The authors would like to thank Nigel Murphy and John Wilkinson of Photometrics U.K. for their continued invaluable help, support and advice throughout the course of this study.

References

[1] S. Amoruso, R. Bruzzese, N. Spinelli, R. Velotta, Characterization of laser-ablation plasmas, J. Phys. B: At. Mol. Opt. Phys, 32 (1999) R131-R172.

[2] E. Tognoni, V. Palleschi, M. Corsi, G. Cristoforetti, Quantitative micro-analysis by laser-induced breakdown spectroscopy: a review of the experimental approaches, Spectrochim. Acta, Part B, 57 (2002) 1115-1130.

[3] R.E. Russo, X.L. Mao, C. Liu, J. Gonzalez, Laser assisted plasma spectrochemistry: laser ablation, J. Anal. At. Spectrom., 19 (2004) 1084-1089.

[4] D.A. Rusak, B.C. Castle, B.W. Smith. J.D. Winefordner, Recent trends and the future of laser-induced plasma spectroscopy, Trends Anal. Chem., 17 (1998) 453-461.

[5] J.M. Vadillo, J.J. Laserna, Laser-induced plasma spectrometry: truly a surface analytical tool, Spectrochim. Acta, Part B, 59 (2004) 147-161.

[6] L.J. Radziemski, From LASER to LIBS, the path of technology development, Spectrochim. Acta, Part B, 57 (2002) 1109-1113.

[7] B. Sallé, P. Mauchien, S. Maurice, Laser-Induced Breakdown Spectroscopy in open-path configuration for the analysis of distant objects, Spectrochim. Acta, Part B, 62 (2007) 739–768.

[8] R. Noll, I. Mönch, O. Klein, A. Lamott, Concept and operating performance of inspection machines for industrial use based on laser-induced breakdown spectroscopy, Spectrochim. Acta, Part B, 60 (2005) 1070-1075.

[9] R. Noll, H. Bette, A. Brysch, M. Kraushaar, I. Mönch, L. Peter, V. Sturm, Laser-induced breakdown spectrometry - applications for production control and quality assurance in the steel industry, Spectrochim. Acta, Part B, 56 (2001) 637-649.

[10] L. Barrette, S. Turmel, On-line iron-ore slurry monitoring for real-time process control of pellet making processes using laser-induced breakdown spectroscopy:

graphitic vs. total carbon detection, Spectrochim. Acta, Part B, 56 (2001) 715-723.

[11] L. St-Onge, E. Kwong, M. Sabsabi, E.B. Vadas, Rapid analysis of liquid formulations containing sodium chloride using laser-induced breakdown spectroscopy, J. Pharm. Biomed. Anal., 36 (2004) 277-284.

[12] R.S. Harmon, F.C. De Lucia, A.W. Miziolek, K.L. McNesby, R.A. Walters, P.D. French, Laser-induced breakdown spectroscopy (LIBS) – an emerging field-portable sensor technology for real-time, in-situ geochemical and environmental analysis, Geochem.: Explor., Environ., Anal., 5 (2005) 21–28.

[13] N.K. Rai, A.K. Rai, LIBS -An Efficient Approach for the Determination of Cr in industrial wastewater, J. Hazard. Mater., In Press, Accepted Manuscript, Available online 22 October 2007.

[14] M.A. Gondal, T. Hussain, Determination of poisonous metals in wastewater collected from paint manufacturing plant using laser-induced breakdown spectroscopy, Talanta, 71 (2007) 73-80.

[15] A. Kaminska, M. Sawczak, K. Komar and G. Śliwiński, Application of the laser ablation for conservation of historical paper documents, Appl. Surf. Sci., 253 (2007) 7860-7864.

[16] A. Brysbaert, K. Melessanaki, D. Anglos, Pigment analysis in Bronze Age Aegean and Eastern Mediterranean painted plaster by laser-induced breakdown spectroscopy (LIBS), J. Archaeo. Sci., 33 (2006) 1095-1104.

[17] F.J. Fortes, M. Cortés, M.D. Simón, L.M. Cabalín, J.J. Laserna, Chronocultural sorting of archaeological bronze objects using laser-induced breakdown spectrometry, Anal. Chim. Acta, 554 (2005) 136-143.

[18] N. M. Shaikh, B. Rashid, S. Hafeez, Y. Jamil, M.A. Baig, Measurement of electron density and temperature of a laser-induced zinc plasma, J. Phys. D: Appl. Phys. 39 (2006) 1384-1391.

[19] A.M. El Sherbini, H. Hegazy and Th.M. El Sherbini, Measurement of electron density utilizing the H_α-line from laser produced plasma in air, Spectrochim. Acta, Part B, 61 (2006) 532-539.

[20] B. Le Drogoff, J. Margot, M. Chaker, M. Sabsabi, O. Barthélemy, T. W. Johnston, S. Laville, F. Vidal, Y. von Kaenel, Temporal characterization of femtosecond laser pulses induced plasma for spectrochemical analysis of aluminum alloys, Spectrochim. Acta, Part B, 56 (2001) 987-1002.

[21] Y. Lee, K. Song, J. Sneddon, Laser Induced Plasmas for Analytical Spectroscopy, in: J. Sneddon, T.L. Thiem, Y. Lee (Eds.), Lasers in Analytical Atomic Spectroscopy,

VCH publishers Inc., New York, 1997, pp. 197-236.

[22] H.C. Liu, X.L. Mao, J.H. Yoo, R.E. Russo, Early phase laser induced plasma diagnostics and mass removal during single-pulse laser ablation of silicon, Spectrochim. Acta, Part B, 54 (1999) 1607-1624.

[23] H.R. Griem, Principles of Plasma Spectroscopy, Cambridge Monographs on Plasma Physics 2, Cambridge University Press, Cambridge,1997.

[24] Laserna M. Milán, J.J. Laserna, Diagnostics of silicon plasmas produced by visible nanosecond laser ablation, Spectrochim. Acta, Part B, 56 (2001) 275-288.

[25] S.S. Harilal, C.V. Bindhu, R.C. Isaac, P.N. Nampoori, C.P.G. Vallabhan, Electron density and temperature measurements in a laser produced carbon plasma, J. Appl. Phys. 82 (1997) 2140-2146.

[26] L. Radziemski, D.A. Cremers, K. Benelli, C. Khoo, R.D. Harris, Use of the vacuum ultraviolet spectral region for laser-induced breakdown spectroscopy-based Martian geology and exploration, Spectrochim. Acta, Part B, 60 (2005) 237-248.

[27] S.S Harilal, C.V Bindhu, M.S.Tillack, F. Najmabadi, A.C. Gaeris, Internal structure and expansion dynamics of laser ablation plumes into ambient gases, J. Appl. Phys. 93 (2003) 2380-2388.

[28] J.S. Cowpe, J.S. Astin, R.D. Pilkington, A.E. Hill, Application of Response Surface Methodology to Laser-Induced Breakdown Spectroscopy: Influences of Hardware Configuration, Spectrocim. Acta, Part B, In Press, Accepted Manuscript.

[29] H.R. Griem, Plasma Spectroscopy, McGraw-Hill Inc., New York, 1964.

[30] CRC Handbook of Chemistry and Physics, CRC Press Inc., Florida, 1988.

[31] A.P. Thorne Spectrophysics, Chapman and Hall Science Paperbacks, London, 1974.

Figure Captions.

Fig. 1: The LIBS apparatus.

Fig. 2a: Si (I) 288.16 nm emission line intensity versus gate delay at atmospheric pressure. Delay swept from 10 – 4010 ns in 200 ns increments, gate width 200 ns, gain 200, 10 spectra accumulated.

Fig. 2b: Si (I) 288.16 nm emission line intensity versus gate delay at $p_a \sim 10^{-5}$ mbar. Delay swept from 10 – 4010 ns in 200 ns increments, gate width 200 ns, gain 200, 10 spectra accumulated.

Fig. 3: Example of Lorentz curve fitted to Si (I) 288.16 nm emission line. Captured spectrum is the grey line, Lorentz fit is the black line. A is represented by the shaded area bound by the curve and y_0.

Fig. 4: Electron temperature versus delay at atmospheric pressure (black squares) and at an ambient pressure of $\sim 10^{-5}$ mbar (white squares). Line of best fit for atmospheric pressure follows an allometric power relation, line of best fit for $p_a \sim 10^{-5}$ mbar follows a double phase exponential decrease. Fit parameters and coefficients of determination are summarized in Table 2.

Fig. 5: Electron density versus delay time at atmospheric pressure (black squares) and at

an ambient pressure of ~ 10^{-5} mbar (white squares). Line of best fit for atmospheric pressure follows an allometric power relation, line of best fit for $p_a \sim 10^{-5}$ mbar follows a double phase exponential decrease. Fit parameters and coefficients of determination are summarized in Table 3.

Fig. 6: Non-dispersed images of plasma plume versus delay time (ns) at atmospheric pressure (top row) compared with ambient pressure of ~10^{-5} mbar (bottom row). The direction of laser propagation is indicated by the white arrow in the first image. The sample surface is perpendicular to the laser beam.

Figure 1:

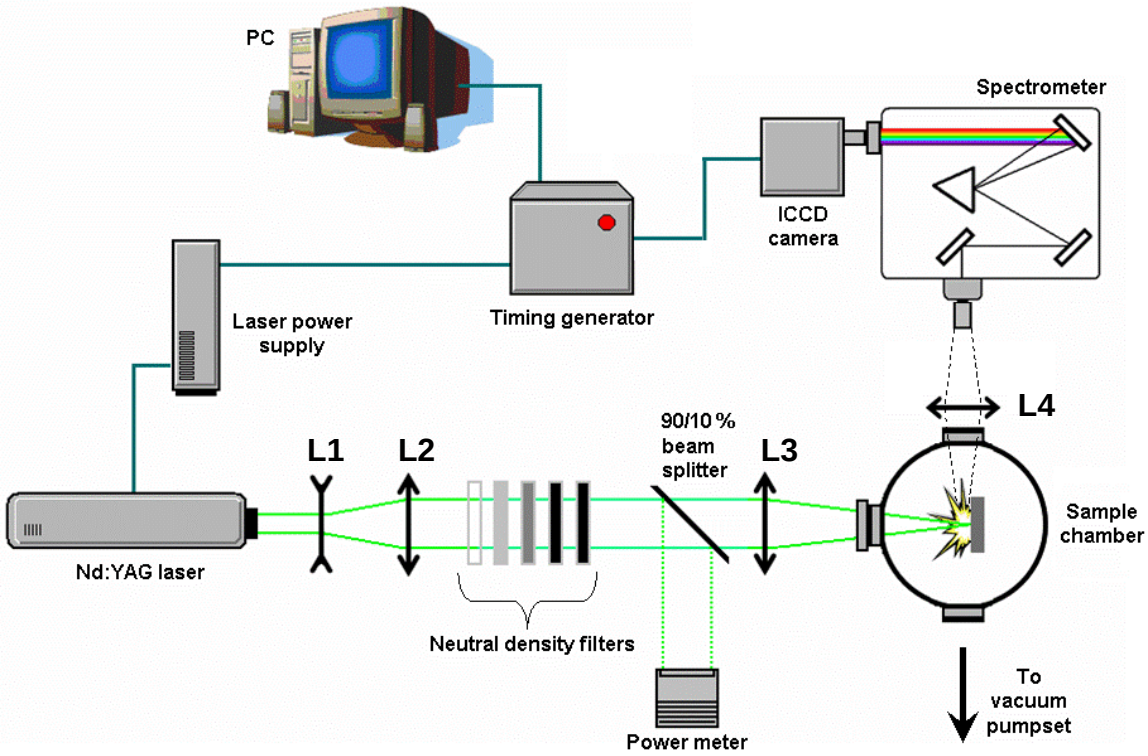
PC
Spectrometer
ICCD
camera
Laser power
supply
Timing generator
L4
90/10 %
beam
splitter
L1
L2
L3
Sample
chamber
Nd:YAG laser
Neutral density filters
To
vacuum
pumpset
Power meter

Figure 2a:

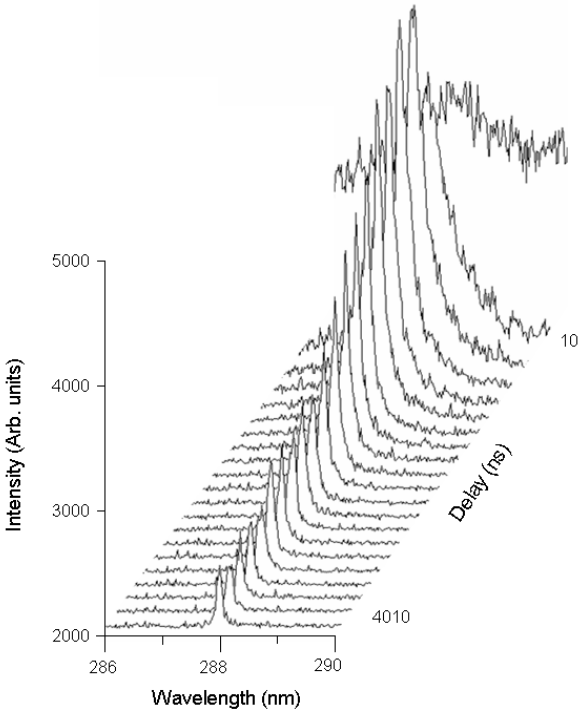
5000
4000
3000
2000
Intensity (Arb. units)
286
288
290
Wavelength (nm)
4010
10
Delay (ns)

Figure 2b:

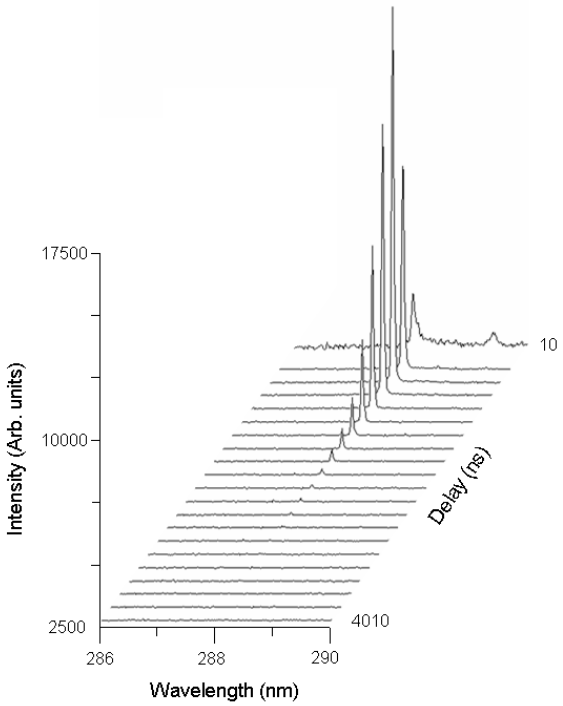
17500
10000
2500
Intensity (Arb. units)
286
288
290
Wavelength (nm)
10
4010
Delay (ns)

Figure 3:

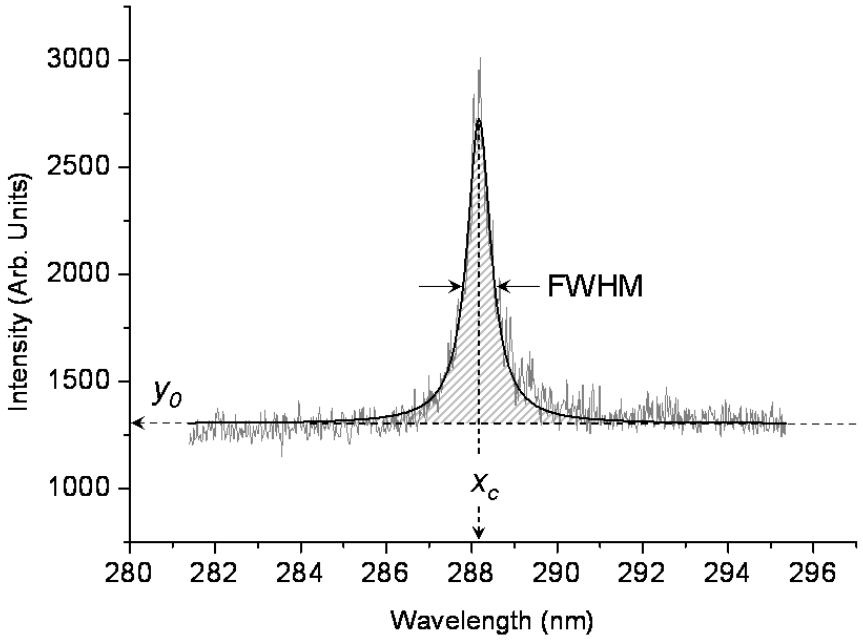
3000
2500
2000
1500
1000
Intensity (Arb. Units)
FWHM
y_0
x_c
280
282
284
286
288
290
292
294
296
Wavelength (nm)

Figure 4:

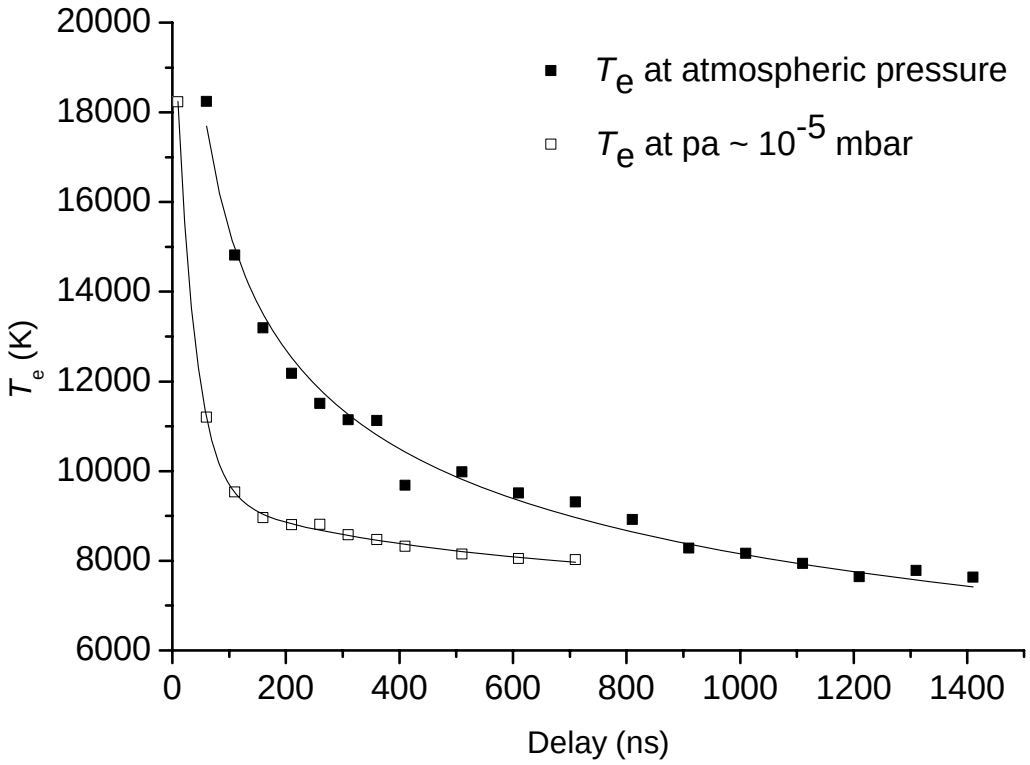
20000
18000
16000
14000
12000
10000
8000
6000
T_e (K)
0
200
400
600
800
1000
1200
1400
Delay (ns)
T_e at atmospheric pressure
T_e at pa ~ 10^{-5} mbar

Figure 5:

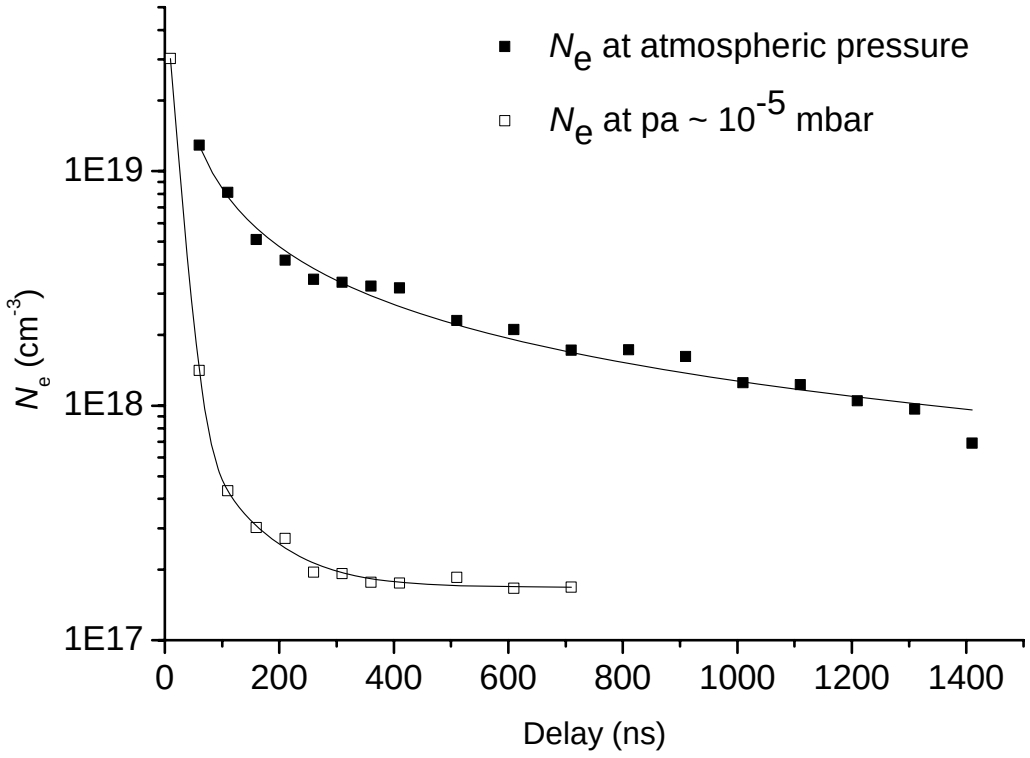
N_e at atmospheric pressure
N_e at pa ~ 10^{-5} mbar
1E19
1E18
1E17
N_e (cm^{-3})
0
200
400
600
800
1000
1200
1400
Delay (ns)

Figure 6: